International Journal of Heat and Mass Transfer 256 (2026) 128033

Contents lists available at ScienceDirect

International Journal of Heat and Mass Transfer

journal homepage: www.elsevier.com/locate/hmt

1D thickness evolution model of cork ablators, including swelling, ablation and erosion

Ciro Salvi [*,1], Oliver Hohn [1], Ali Gülhan [1]

German Aerospace Center (DLR), Linder Höhe, 51147, Köln, Germany

ARTICLE INFO

Keywords:
Arc-heated wind tunnel
Cork-based ablator
Ablation
Recession
Swelling
Erosion
LPT

ABSTRACT

A one-dimensional mathematical framework is developed to describe the thickness evolution—swelling and recession—of cork samples in high enthalpy flows, in the arc-heated wind tunnel L2K. The model is formulated to account for swelling effect, constant long-term recession rate, particle-induced erosion, and post-erosion swelling—that is swelling enhancement after char removal by particle impact. Particle effects were considered as they are particularly important for the simulation of Martian entry during dust storms, and might be useful for other applications. The model is fitted to experimental time-resolved recession data measured with laser-sheet profile tracking (LPT), with the goal of determining material-specific parameters in different flow conditions, also in the presence of particles. The results demonstrate that the approach captures key flow-structure interaction phenomena and reproduces experimental and numerical reference data within acceptable error margins: the never-theorized phenomenon called post-erosion swelling is thereby confirmed. This establishes the model as a computationally efficient foundation for further extensions to parametric approaches for material response prediction, in high-enthalpy flows.

1. Introduction

Ablative thermal protection systems (TPS) provide a simple and reliable protection from high heat fluxes for limited times. They are used in a wide range of applications in hypersonic flight and spaceflight, as they provide a cost-effective option for missions designed for non-reuse.

An ablative heat shield works by sacrificial material removal to protect the underlying structure from extreme heating. Ablative materials are able to absorb and dissipate heat through endothermic processes, thanks to their peculiar chemical composition—the majority of ablators for re-entry application is made of a dispersed phase, bound by a matrix. Different matrices and dispersed phases confer different properties to the ablator, in terms of heat ablation efficiency, thermal conductivity, density, etc. Commonly used ablative materials are composed of:

- *Carbon fibre & phenolic resin*, such as ZURAM [1] and PICA (used in Mars Science Laboratory MSL [2], SpaceX Dragon [3], and Dragonfly [4]).
- *Fibreglass & epoxy resin*, such as AVCOAT (used in Apollo [5] and Artemis [6]).
- *Silica fibre & phenolic resin*, such as SLA-561V (used in Mars Pathfinder [7]).
- *Cork & phenolic resin*, such as Norcoat Liège (used in ExoMars Schiaparelli [8]) and P50 (used in ESA-IXV [9,10]).

The characterization of ablative materials' response in relevant environments—such as long-duration high-enthalpy wind tunnels—provides useful tools and parameters allowing the predictability of the in-flight material behaviour. The thickness evolution measurement (usually referred to as *recession-* or *erosion measurement* in the literature) has always been a challenge during tests in high-enthalpy wind tunnels, due to the difficulty of working with high-enthalpy flows, the unsuitability of intrusive techniques, and the facilities' limited optical accessibility. In a recent work [11], thickness evolution measurements were performed by an innovative time-resolved technique named laser-sheet profile tracking (LPT), that provides 1D resolution of the thickness evolution, along the sample surface's diameter. LPT was applied to study P50 cork samples evolution in several particle-laden high-enthalpy flow conditions [12–14]. This research is the result of a collaboration between the German Aerospace Center (DLR) and the NASA Ames Research Center that focuses on studying the effects of particle-induced erosion on heat shields, during Martian entry in a global dust storm [15,16].

* Corresponding author.
E-mail addresses: ciro.salvi@dlr.de (C. Salvi), oliver.hohn@dlr.de (O. Hohn), ali.guelhan@dlr.de (A. Gülhan).
[1] Supersonic and Hypersonic Technologies Department.

https://doi.org/10.1016/j.ijheatmasstransfer.2025.128033
Received 29 August 2025; Received in revised form 15 October 2025; Accepted 23 October 2025

Researchers aim to develop validated mathematical models capable of describing different materials' behaviours, thereby enabling cost-effective predictions of heat shield performance under the extreme conditions of atmospheric entry. The present work introduces a novel simplified one-dimensional parametric model designed to interpret the response of cork-based ablators in high-enthalpy flows. This approach ultimately seeks to identify material response coefficients across a wide range of heat flux conditions for predictive applications. The model is valid for cork-based ablators and it includes the effects of swelling, ablation, particle-induced erosion, and post-erosion swelling—a newly identified phenomenon—which are described in Section 2. As a proof of concept, the model is fitted on the experimental LPT data reported in [11] to determine material response coefficients.

Following sections describe the theory behind thickness evolution, the hypotheses and formulations behind the 1D model, the test setup, and the fitting results.

2. Thickness evolution

In hypersonic flows, strong bow-shocks and temperature gradients develop in the vicinity of material surfaces. This causes high heat flux values that require careful engineering analysis to ultimately grant mission safety, for aerospace applications. The typical ablation process of ablative TPS is based on the controlled material degradation favoured by endothermic reactions:

1. As the material is exposed to high heat fluxes, the binder in the outer layer starts decomposing through **pyrolysis**—that is the endothermic chemical breakdown of long polymeric chains [17]. The pyrolysis front moves inward, affecting the virgin material, which is gradually reduced with time.
2. Pyrolysis produces gases that blow outward. **Outgassing** provides transpiration cooling effects by forming a boundary layer that shields the surface, and may also push the shock away from the surface, reducing heat transfer. Furthermore, these gases can cause material swelling in some types of ablators.
3. The remaining—possibly swollen—solid phase after pyrolysis constitutes a **char** layer, that is a porous structure with insulating properties that slows heat conduction.
4. Finally, the surface material is subject to **ablation** caused by melting, sublimation, spallation, shear erosion and chemical reactions (e. g. oxidation) [18–20]; this process is ideally endothermic, and it carries thermal energy away, therefore cooling the surface by loss of hot mass.
5. The mass loss causes material **recession**.

The combination of endothermic reactions, surface cooling, thermal insulation, and mass loss during ablation, makes ablative materials an ideal cost-effective choice for protection against high heat fluxes [21].

Terms related to ablation processes are often used inconsistently in the literature, and it is therefore important to clarify their distinct meanings:

- **Swelling** defines the expansion of the material, typically caused by outgassing, charring and thermal expansion.
- **Ablation** describes the mass loss due to high thermal and mechanical loads. It encompasses the effects of:
  - Pyrolysis (material decomposition),
  - Phase change (melting, evaporation, sublimation),
  - Spallation (sudden mechanical removal of surface chunks due to thermomechanical stress),
  - Shear erosion (gradual removal of material by continuous shear forces),
  - Chemical reactions with the flow (for example, oxidation, or reactions with free radicals),
  - Particle-induced erosion (sudden mechanical removal of the surface due to particle impact).
- **Recession** is the progressive loss of material that results in a net backward movement of the probe surface—it happens when the ablation rate is higher than the swelling rate.
- **Thickness Evolution** is the combination of swelling and ablation. According to the convention used in this manuscript, it is positive in case of overall recession, and negative in case of prevalent swelling. It is therefore a more general term with respect to recession—which means positive evolution.

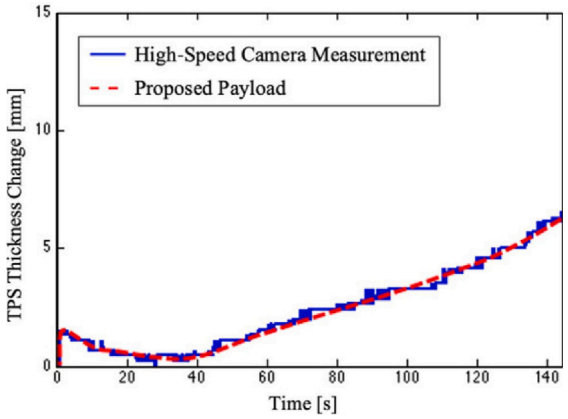

Fig. 1. Typical cork-based ablator evolution process.
Source: From [22]

In this work, the term thickness evolution is sometimes shortened to *evolution*, and particle-induced erosion is referred to simply as *erosion*—not to be confused with shear erosion.

As mentioned in [9,22], cork-based ablators present a non-linear behaviour at the beginning of the test where they experience swelling: samples thickness evolves to negative values. Then, ablation processes start, and recession gains prominence over swelling. The long-term recession rate is constant, and therefore the evolution's slope is constant. The typical evolution process of cork-based ablator is reported in Fig. 1, taken from [22],

2.1. Erosion rate modelling

A particle-laden two-phase flow impacting a surface causes erosion. In [23,24] erosion is described as a material-dependent process that starts with a transient and stabilizes in a quasi-steady phase with constant erosion rate.

Erosion is due to the combination of multiple effects, such as the cutting wear and the deformation wear, as described in [25,26]. The cutting wear is prominent when the impact angle is close to zero (i. e. the particle moves almost parallel to the surface), while the deformation wear gains importance when the impact angle is close to 90° (i. e. particles' trajectories are almost perpendicular to the surface). In this work's scenario, the cutting wear is considered negligible, with respect to the deformation wear, as the wind tunnel flow is almost perpendicular to the sample surface.

The main contributions to erosion are given by particle size d_p, mass m_p, velocity v_p, impact angle α, and material hardness H_v, as described by [25,27]. In the mentioned works, the Oka erosion model was used [28,29], which relates the mass loss Δm to particle and material characteristics:

$$\frac{\Delta m}{\Delta m_p} = c_1 H_v^{c_2} v_p^{c_3} d_p^{c_4} (\sin\alpha)^{c_5} \tag{1}$$

valid for α close to 90°, where c_i are the model's coefficients. In specific studies related to Martian entry conditions and cork modelling, similar material-dependent erosion models were reported [15,30,31], highlighting the dependency of the surface erosion depth Y^ϵ on the impact crater and penetration depth, that in turn depend on particle density ρ_p, total particle number N_p, α, v_p, and d_p:

$$Y^\epsilon = c_6 v_p^{c_7} d_p^{c_8} \rho_p^{c_9} N_p (\sin\alpha)^{c_5} \tag{2}$$

According to this equation, one could relate erosion to particle's kinetic energy or momentum, depending on the model coefficients c_i—which are material- and flow condition-specific.

The **erosion rate**—defined as the contribution of particles alone to the thickness evolution rate—can be evaluated by differentiating Eq. (2). Assuming no change in particle properties, and constant velocity:

$$\frac{dY^\epsilon(t)}{dt} = c_{10} \frac{dN_p(t)}{dt} \tag{3}$$

where $\frac{dN_p(t)}{dt}$ is the particle flux, defining the particle number per unit time.

In this work, particles were counted—exploiting a laser sheet used for particle image velocimetry (PIV)—within a defined region of interest (RoI) upstream of each sample, with the aims of characterizing the particle flux nature, and relating the particle count to the time-resolved surface erosion, as described in Section 4. Counting was performed within a rectangular RoI upstream of the sample, that lays in the wind tunnel free stream (thus excluding the shock layer), with a width Δx_{RoI} = 17.8 mm, and a height of 34.9 mm. The investigated RoI was selected based on the presence of high-quality raw data, favourable illumination conditions, and sufficient distance from the sample surface to minimize the inclusion of particles originating from the sample.

Thanks to the nature of the RoI—according to its location and its small height—it is reasonable to assume that the vertical component of particle velocity within this region is negligible. Therefore, it is possible to estimate the time it takes particles to traverse the whole RoI Δt_{RoI}, as:

$$\Delta t_{RoI} = \frac{\Delta x_{RoI}}{|v_p|} \tag{4}$$

The particle flux $\frac{dN_p}{dt}$ can be related to the particle count n_p, assuming homogeneous velocity field and constant particle velocity v_p; this assumption is reasonable as the RoI lays in the free stream. Assuming that the particle seeding is homogeneous, the counted particles can be used to obtain the overall particle number in any wanted volume in front of the probe simply by scaling with a constant c_{11}:

$$\frac{dN_p}{dt} \approx c_{11} \frac{n_p(t)}{\Delta t_{RoI}} = c_{11} |v_p| \frac{n_p(t)}{\Delta x_{RoI}} \tag{5}$$

According to the mentioned assumptions, all quantities above except n_p are constant. Substituting Eq. (5) in Eq. (3), and collecting all constants in one single proportionality factor A, one finds:

$$\frac{dY^\epsilon}{dt} = A n_p(t) \tag{6}$$

A depends on the particle- and material-related properties, particle velocity, and laser sheet volume. Combining Eq. (2) and Eq. (6) one finds:

$$A = c_6 c_{11} v_p^{c_7+1} d_p^{c_8} \rho_p^{c_9} (\sin\alpha)^{c_5} \Delta x_{RoI}^{-1} \tag{7}$$

where c_i are the model's constants.

In summary, the erosion rate is proportional to the particle count, assuming constant and homogeneous particle velocity, constant particle properties (density and size), constant material properties, homogeneous seeding, and quasi-perpendicular impact.

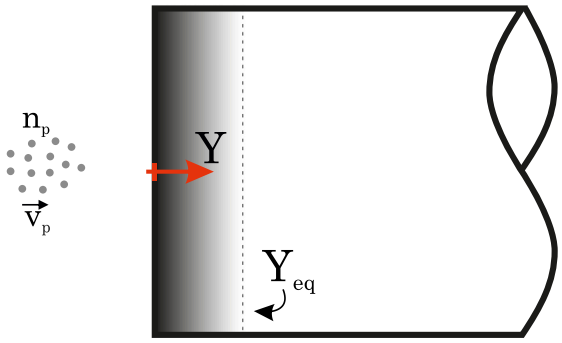

Fig. 2. 1D surface evolution model.

3. Mathematical model

The sample thickness evolution can be described by the sample surface's position $Y(t)$, with $Y(t_0)$ = 0 mm. In particular, negative Y is associated to swelling, while positive Y to recession—according to the convention used in this paper—as presented in Fig. 2. The model is 1D.

The main assumptions of the model are:

1. The evolution rate $\frac{dY}{dt}$ is dependent on several components; the first is proportional to the distance between the sample surface Y from a general equilibrium surface Y_{eq}.

$$\left(\frac{dY}{dt}\right)_1 = -k\left(Y(t) - Y_{eq}(t)\right) = -k\Delta Y \tag{8}$$

   One can for instance visualize ΔY as directly related to the surface layer, where the virgin cork transforms to pyrolysed material and ultimately char, before being ablated away. ΔY does not necessarily coincide with the charring thickness.
2. The second component of the evolution rate is provided by particle-induced erosion. This effect is directly proportional to the number of particles $n_p(t)$, as demonstrated in Eq. (6), assuming constant and homogeneous particle velocity, constant particle properties (density and size), constant material properties, homogeneous seeding, and quasi-perpendicular impact.

$$\left(\frac{dY}{dt}\right)_2 = \frac{dY^\epsilon}{dt} = A\, n_p(t) \tag{9}$$

3. The total evolution rate is the sum of the mentioned effects, assuming linearity.

$$\frac{dY}{dt} = \left(\frac{dY}{dt}\right)_1 + \left(\frac{dY}{dt}\right)_2 = -k\left(Y(t) - Y_{eq}(t)\right) + A\, n_p(t) \tag{10}$$

With k depending on the flow condition (stagnation temperature, mass flow rate, enthalpy) and the material response (charring thickness, recession rate, swelling rate), and A depending on the particle momentum and the material properties, as for Eq. (7). Both proportionality factors are positive.

The equilibrium surface location Y_{eq} can be modelled in different ways, depending on the expected material behaviour. It is reasonable to hypothesize that Y_{eq} is time-varying, depending on the flow condition and on the probe material. In this configuration, Y_{eq} depends mainly on swelling, recession, and erosion effects. Hypothesizing linearity between these phenomena:

$$Y_{eq}(t) = Y_{eq}^\sigma(t) + Y_{eq}^\rho(t) + Y_{eq}^\epsilon(t) \tag{11}$$

where σ, ρ, and ϵ refer to swelling, recession, and erosion effects, respectively. The negative starting value of Y_{eq} causes Y to move to negative values (which represents swelling with decreasing exponential trend) at the beginning of the test, and the positive constant slope leads

the system to a positive constant recession rate on the long term, in agreement with the results presented in [9,22]. For this reason, the time evolution of the equilibrium surface can be modelled as a straight line with positive slope and negative Y-intercept. In this configuration:

$$Y_{eq}^{\sigma}(t) + Y_{eq}^{\rho}(t) = at + b \tag{12}$$

where $a > 0$ and $b < 0$.

Particles were observed to have a direct effect on Y_{eq}. Their impacts drive Y to jump sharply towards positive values (i.e., particle-induced erosion, modelled by An_p), violently striping the surface char away, directly affecting $\Delta Y = Y - Y_{eq}$. As the virgin layer is exposed, Y_{eq} is pushed back towards negative values, as the swelling phenomenon is favoured. In other words, the virgin material is exposed to the flow and "wants" to swell. At this stage of the study one can hypothesize that Y_{eq} is decreased by the same amount that the probe has eroded due to particles, that is:

$$Y_{eq}^{\varepsilon}(t) = -\int_0^t A\, n_p(\tau)\, d\tau \tag{13}$$

The negative sign highlights that this effect favours swelling. This phenomenon was never reported in the literature and is defined as post-erosion swelling.

In current form, a severe particle burst can lead to a sharp decrease in ΔY, which results in a negative Y rate with large magnitude. If the effect is pronounced, the magnitude could become non-physically high, causing a swelling rate higher than the swelling rate at the beginning of the test—that is a physical limit. For this reason a constraint on Y_{eq} needs to be imposed such that $\Delta Y(t)$ can never be larger than $\Delta Y(t_0)$:

$$\Delta Y(t) \leq \Delta Y(t_0) = -b \qquad \Rightarrow \qquad Y_{eq}(t) \geq Y(t) + b \tag{14}$$

The model is formulated as a constrained linear, first-order, inhomogeneous ODE with a time-dependent forcing term involving an integral, solvable through the corresponding initial value problem (IVP):

$$\begin{cases} \frac{dY}{dt} = -k\left(Y(t) - at - b + \int_0^t A\, n_p(\tau)\, d\tau\right) + A\, n_p(t) \\ Y(t_0) = 0 \text{ mm} \end{cases} \tag{15}$$

The IVP's general solution, without the mathematical constraint proposed in Eq. (14) yields:

$$\begin{aligned} Y(t) &= e^{-kt}\left[Y_0 + \int_0^t e^{ks}\left(k\left(as + b - A\int_0^s n_p(\tau)d\tau\right) + An_p(s)\right)ds\right] \\ &= e^{-kt}\Bigg[\underbrace{Y_0}_{\text{initial condition}} + \underbrace{ka\int_0^t se^{ks}ds}_{\text{recession}} + \underbrace{kb\int_0^t e^{ks}ds}_{\text{swelling}} + \\ &\quad \underbrace{-kA\int_0^t e^{ks}\left(\int_0^s n_p(\tau)d\tau\right)ds}_{\text{post-erosion swelling}} + \underbrace{A\int_0^t e^{ks}n_p(s)ds}_{\text{particle-induced erosion}}\Bigg] \end{aligned} \tag{16}$$

In its explicit form:

$$\begin{aligned} Y(t) = &\underbrace{a\left(t - \frac{1-e^{-kt}}{k}\right)}_{\text{recession}} + \underbrace{b\left(1-e^{-kt}\right)}_{\text{swelling}} + \\ &\underbrace{-A\int_0^t n_p(s)\left(1-e^{-k(t-s)}\right)ds}_{\text{post-erosion swelling}} + \underbrace{A\int_0^t n_p(s)e^{-k(t-s)}ds}_{\text{particle-induced erosion}} \end{aligned} \tag{17}$$

With this formulation, the solution depends on four terms, each associated to the four effects:

- **Recession** contributes with an exponential decay towards a linear trend with slope a, which is the long-term recession rate.
- **Swelling** contributes with an exponential decay with initial value b.
- **Post-erosion swelling** is caused by the cumulative exposure to particles and it is represented by the convolution of the particle flux $n_p(t)$ with the kernel $h_1(t) = 1 - e^{-kt}$, which accumulates particle effects over time with a saturating memory effect.

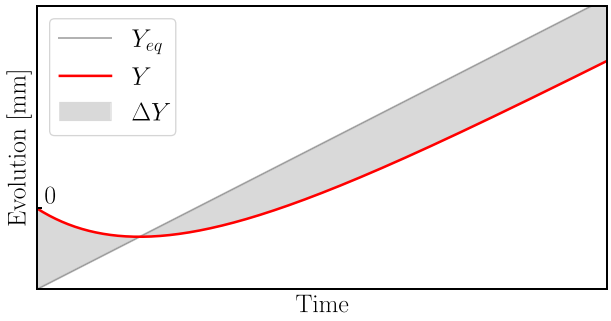

Fig. 3. Generic response without particles.

- **Particle-induced erosion** is the instantaneous reaction to the particle flux $n_p(t)$ and it is represented by the convolution of $n_p(t)$ with the kernel $h_2(t) = e^{-kt}$, representing an exponentially weighted instantaneous impact of particles.

Note that the explicit solution is useful for understanding each effect's contribution, but it does not consider the constraint proposed in Eq. (14). Enforcing such constraint during the fitting process requires numerical integration.

3.1. Model discussion

The model presented in this work serves as a tool for identifying material parameters in response to high enthalpy flows. Unlike approaches that rely on detailed chemical reaction mechanisms or fully deterministic simulations—such as the DLR's FAST tool [32], the NASA's LAURA code [33,34], or other models [35]—the present model is grounded in the experimental evidence of cork behaviour under relevant thermal and aerodynamic loads. This strategy offers notable advantages: it is relatively straightforward to implement and can provide reliable predictions if properly validated against experimental data. However, a significant limitation is the requirement for a sufficiently comprehensive database linking flow conditions to material response; currently, the lack of such data limits predictive accuracy for conditions different from those investigated, highlighting an important avenue for future experimental and validation efforts.

Qualitative simulations of the described 1D model are here presented, with the aim of guiding the reader towards a clearer understanding of its behaviour. In Fig. 3, the model response is shown when no particles are considered ($n_p = 0$). The dark grey line represents the equilibrium surface evolution, $Y_{eq}(t) = at + b$ (from Eq. (12)); the red line represents the model solution, $Y(t)$; and the shaded region corresponds to ΔY, which—according to Eq. (8)—is proportional (through the factor $-k$) to the first derivative of Y when no particles are present. In case of no particles:

- Since $-\Delta Y(t_0) = b < 0$, at $t_0 = 0$ s the surface Y is pulled towards negative values (this represents the swelling behaviour).
- In the following few seconds, $-\Delta Y$ is negative, with decreasing magnitude: the first derivative of Y is negative-increasing.
- At the inversion point, when ΔY is zero, Y has a stationary point.
- After the stationary point, $-\Delta Y$ increases up to a constant: combining the explicit solution presented in Eq. (17) with Eq. (12), one finds that—for long testing times—the first derivative of Y tends to a. In other words, the long-term slope of the red line—which coincides with the long-term recession rate—is equal to a. This aspect is convenient while fitting the mathematical model to the data, as the recession rate is easily retrieved during the process.

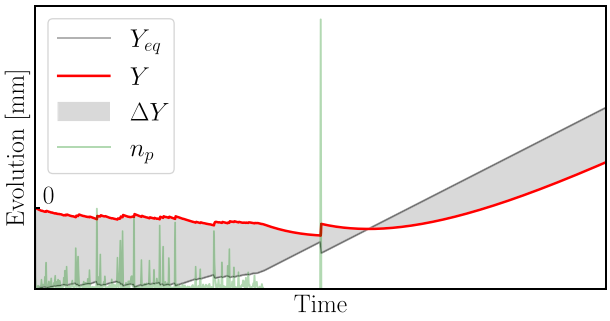

Fig. 4. Generic response with particles.

In Fig. 4, a generic simulation with particles is reported; particles are randomly simulated and plotted as a green line. In this case, $Y_{eq}(t)$ includes the post-erosion swelling contribution, as reported in Eq. (13):

- $Y_{eq}(t)$ is not a straight line as in the case without particles: its value is pulled towards negative values—thus favouring swelling—due to the post-erosion swelling effect.
- At the same time, particles give a positive contribution to the derivative of Y, according to Eq. (9). For this reason, Y increases in the presence of particle bursts.
- Particle-induced erosion and post-erosion swelling are two counteracting phenomena: depending on the particle number, one effect may prevail. In fact, in the presence of particles, the derivative of Y is not always positive, even though erosion takes place.
- The constraint presented in Eq. (14) forces ΔY—the grey region—below $\Delta Y(t_0)$, to avoid representing a too-high non-physical swelling value.
- After the particle flow is terminated, $Y_{eq}(t)$ resumes its linear behaviour, and Y responds nominally as in the case without particles.

The model parameters a, b, and k have a specific influence on the system response, and they depend on material properties and flow condition. Their effects are illustrated in Figs. 5 to 7, where each parameter is varied individually, considering the particle-free case for simplicity:

- The parameter a is the slope of Y_{eq} and the long-term recession rate, thus defining the slope of Y at the end of the test.
- The parameter b is the Y-intercept of Y_{eq}, and it has a direct effect on the swelling amount, i. e. to what extent the surface Y moves towards negative values at the beginning of the test.
- The parameter k is the system's stiffness and it represents how fast the material reacts to the imposed forcing term ΔY. Response time and swelling amount depend on this parameter.

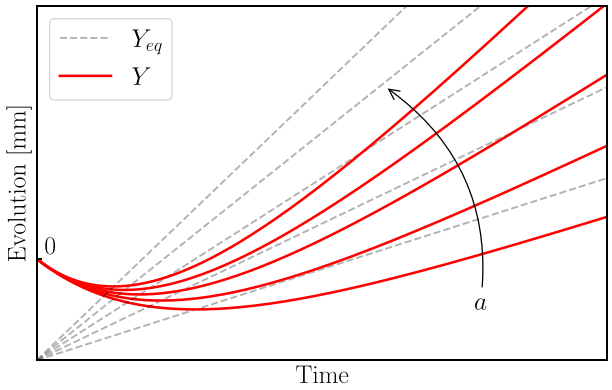

Fig. 5. Influence of long-term recession rate a.

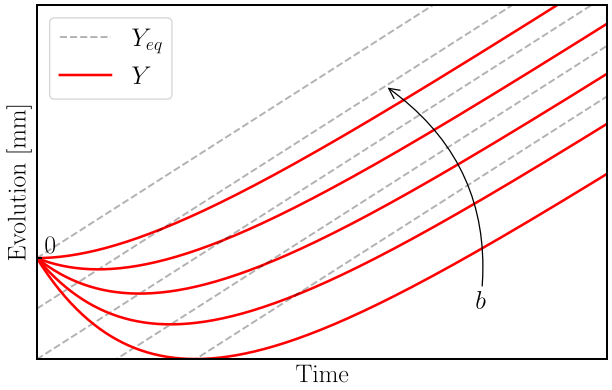

Fig. 6. Influence of swelling parameter b.

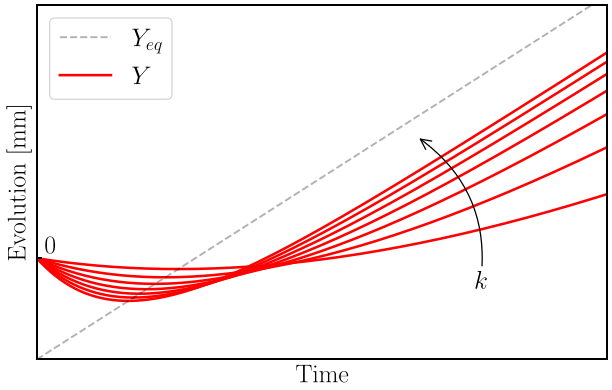

Fig. 7. Influence of system stiffness k.

4. Experimental setup

A sketch of the experimental setup in the L2K test section is reported in Fig. 8. This is the same setup used in [11,13]. The coordinate system is defined as follows: the x-axis coincides with the nozzle symmetry axis, it originates at the nozzle exit, and x values are positive downstream (towards right, referring to the picture); the y-axis defines the transversal direction, it originates on flow axis, and y values increment towards the top of the wind tunnel; both axes belong to the laser sheet plane. Note that the sCMOS is represented on a wrong plane for schematic visualization purposes only; same for the particles injection, which happens on the horizontal mid-plane of the settling chamber. In practice, both the seeding generator and the sCMOS camera are positioned in the xz plane.

4.1. Arc-heated facility L2K

L2K is an arc-heated continuous-flow high-enthalpy wind tunnel suited for TPS materials testing and components' demisability tests, as it can provide high heat fluxes for long testing times, at the expense of aerodynamic properties characterization: the low density environment causes Reynolds number to be too low compared to atmospheric entry. In such conditions it is important to consider a reacting non-equilibrium flow. L2K reservoir is energized by a 1.4 MW Huels-type arc heater which grants the flow a high specific enthalpy thanks to the electrical discharge. Flow conditions can be varied with different degrees of freedom, such as mass flow rate, reservoir pressure, nozzle exit diameter, sample position, and chamber background pressure, which grant a wide range of operating conditions of the testing facility. Thanks to the use of

Table 1
Flow conditions FC. *P* and *nP* superscripts indicate the FC with and without particles respectively. The mass flow rates are equal for all FC.

Parameter	FCI^{nP}	$FCII^{nP}$	FCI^{P}	$FCII^{P}$
Reservoir pressure, [hPa]	790	930	790	930
MgO Particles	✗	✗	✓	✓
Predicted specific enthalpy[a], [MJ/kg]	5.6	9.2	5.6	9.2
Predicted reservoir temperature[a], [K]	2815	3283	2815	3283
Total mass flow rate, [g/s]	41.2			
Mass flow rate CO_2 (97%), [g/s]	$38^{hot}+2^{BP}$			
Mass flow rate N_2 (3%), [g/s]	1.2^{hot}			

[a] Estimated with quasi-1D flow solver NATA [37].

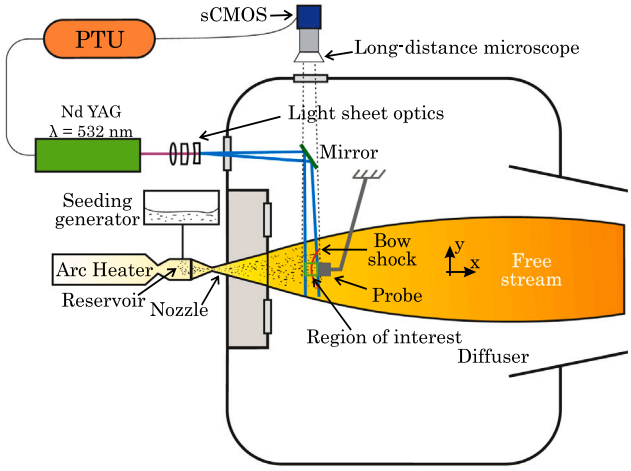

Fig. 8. Experimental setup sketch, in the L2K test section. The reported axes originate on the flow axis, at the nozzle exit location. In practice, both the seeding generator and the sCMOS camera are positioned in the *xz* plane.

conical nozzles, the heat flux varies also on flow axis. A broad selection of intrusive and non-intrusive measurement techniques can be used (for instance, thermocouples, infrared cameras, pyrometers, Pitot probes, Tunable Diode Laser Absorption Spectroscopy or TDLAS, Laser Induced Fluorescence or LIF, Fourier Transform Infrared spectroscopy or FTIR, PIV, LPT).

The analysed flow conditions (FC) are defined by DLR in the post-flight analysis of ESA ExoMars 2016 mission [36], and are reported in Table 1. Here, the superscript "*P*" indicates the flow condition with particles, while the superscript "*nP*" indicates no particles in the flow. The wind tunnel flow represents a slightly simplified Martian atmosphere and its composition is 97% CO_2 and 3% N_2. To generate the particle-laden flow, a seeding generator inserts MgO particles in the L2K flow upstream of the nozzle expansion. The seeding generator is a pressurized vessel working with a bypass (BP): to keep the mass flow rate as specified in Table 1, 38 g/s of CO_2 are heated in the arc-heater together with 1.2 g/s of N_2 (superscript "*hot*"), while 2 g/s of CO_2 are used for collecting the particles inside the pressurized vessel (superscript "*BP*"). Particles of magnesium oxide (MgO) are stored inside the pressurized vessel. The used particles are LUVOMAG®M SF. The producer assures that 95% of them range between 1 μm and 3 μm.

Fig. 9 shows the test chamber during a particle-laden flow experiment, as captured by the video monitoring cameras. The flow enters from the left, with the sample held in position by a cooled support. When particles are present, a bright red–orange bow shock forms ahead of the sample, followed by a blue–greenish wake containing ablation products downstream. The green light-sheet used for in-situ evolution measurements and particle count (Sections 4.3 and 4.4) is also visible, illuminating both the sample and the particles suspended in the flow.

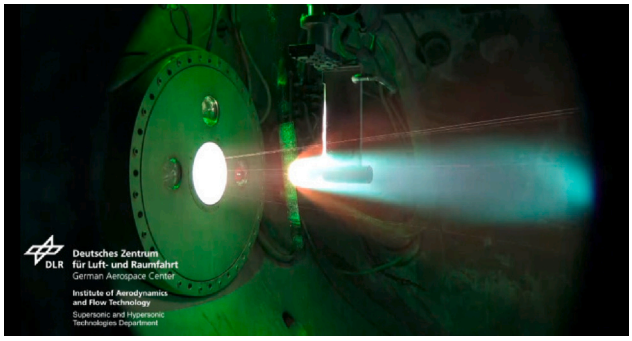

Fig. 9. L2K test chamber during a particle-laden flow experiment, on a cork sample. The green light-sheet is used for in-situ evolution measurements and particle count.

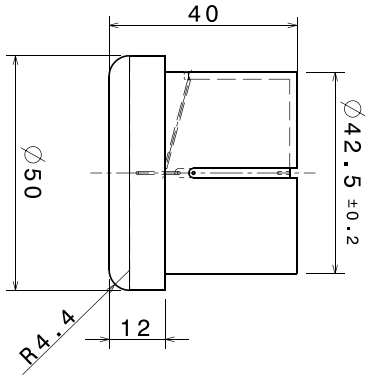

Fig. 10. Sample geometry. The left side faces the flow; the right thinner side is used to position the thermocouples and to connect to the cooled support.

4.2. P50 cork samples

The samples used in this study all have the same characteristics, to address the repeatability of the tests in the L2K wind tunnel. All tests are executed in the same way, and the only variables between tests are the reservoir pressure and the presence of particles, as reported in Table 1. The sample geometry is presented in Fig. 10. The material is P50 cork, from the company Amorim Cork Solutions.[2]

During a wind tunnel test the sample is positioned on the flow axis after the flow is stabilized, at a distance of $x = 300$ mm from nozzle exit. At this location, the expected[3] cold-wall heat flux and stagnation

[2] https://amorimcorksolutions.com/en-us/materials-applications/aerospace/

[3] These values are computed numerically with the DLR-TAU solver, with the same setup used in [13].

Table 2
Test parameters for different flow conditions.

Flow condition	Sample position	Residence time	Stagnation heat flux[a]	Stagnation pressure[a]
$FCI^{P/nP}$	300 mm	60 s	280 kW/m^2	1280 Pa
$FCII^{P/nP}$	300 mm	60 s	490 kW/m^2	1510 Pa

[a] Predicted with CFD.

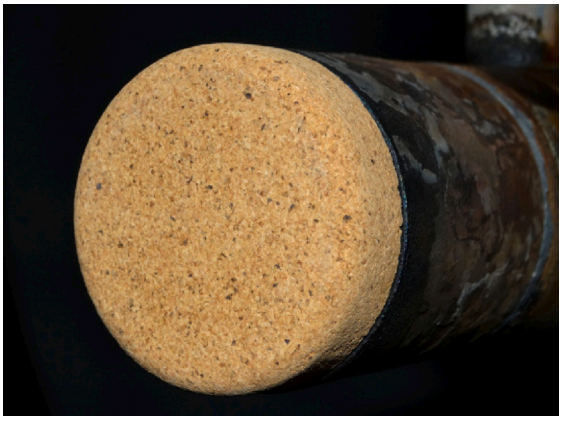

Fig. 11. Sample before testing.

pressure are reported in Table 2. The heat flux values are comparable to the ones calculated in [38], for the MSL entry module. A total of 10 tests are performed, namely 2 tests per each FCs^{nP} and 3 per each FCs^{P}, to assess repeatability. Peculiar phenomena (later discussed) are observed when particles are fed in the flow. A picture of the sample installed in the wind tunnel before the test is shown in Fig. 11.

Snapshots from video monitoring are shown in Fig. 12 to qualitatively show the sample behaviour during test in the different flow conditions. One can observe the particles' erosive effect that causes the disruption of cork charring cells, and the effect of the higher enthalpy of $FCII^{P/nP}$ that makes the sample surface hotter, thus brighter.

4.3. Laser-sheet profile tracking (LPT)

The samples evolution was measured with an innovative technique based on image processing, and described in [11], named laser-sheet profile tracking (LPT). The laser sheet sketched in Fig. 8 highlights the probe's mid-profile, that can be tracked over time. During the test, the camera records multiple pictures at a defined frame rate—limited by the laser repetition rate—building up a time series. The frame rate of the system is 15 Hz, thus 900 frames per minute. The profile P_r is created by the intersection of the sample with the light-sheet plane containing the sample's axial-symmetry axis. The algorithm finds the axial position of the profile for every pixel in y. In other words: $x = P_r(y,t)$, as can be seen in Fig. 13, from [11]. By comparing $P_r(t)$ with $P_{r,0} = P_r(t_0 = 0s)$, one can measure the probe's evolution on the mid plane of the sample. Thanks to the experiment setup construction, the displacement of the profile in x coincides with the evolution of the profile, which is time- and y-dependent. To evaluate the local evolution E, the profile at the beginning of the test ($t_0 = 0$ s) is subtracted from each profile:

$$E(y,t) = P_r(y,t) - P_r(y,t_0) = P_r(y,t) - P_{r,0} \tag{18}$$

Thanks to the massive structure of the L2K wind tunnel and the relatively short testing times, no laser misalignments and no probe support deformation were observed.

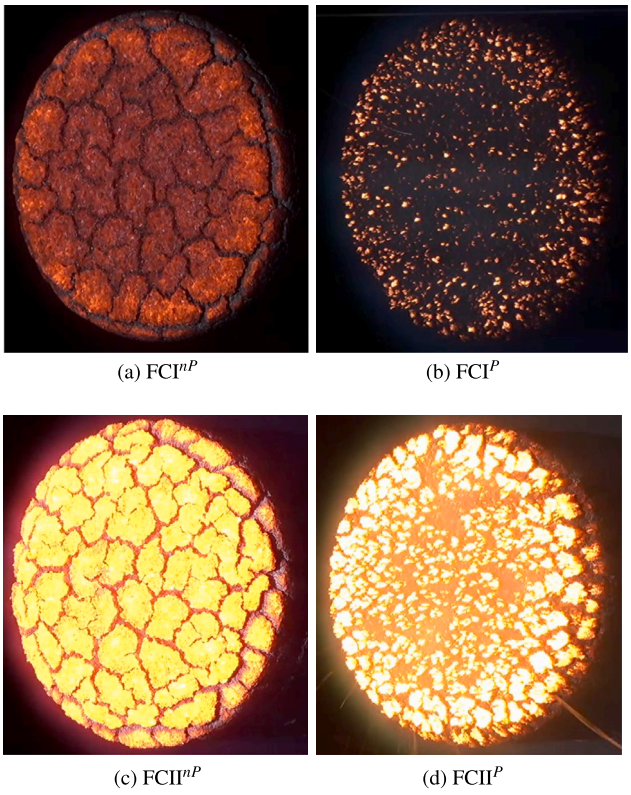

Fig. 12. Samples during testing in different flow conditions.

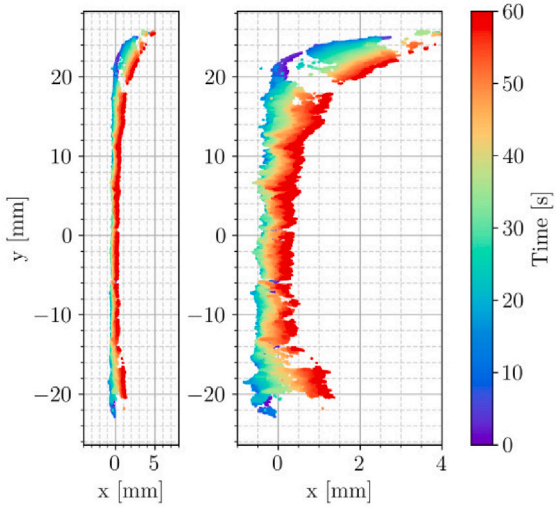

Fig. 13. Mid-plane profile evolution, colour-ordered over time. The two plots present the same data, one with equal axes aspect ratio (left), and one with stretched x to better appreciate the profile evolution.
Source: From [11].

4.4. Particle count

Particles highlighted by the light sheet were counted with a built-in function from the DaVis software used for recording [39], named *Particle Counter*, after the raw images were processed by:

1. Cropping the figure according to the selected RoI (described in Section 2.1).
2. Setting all values below a threshold intensity to 0—the threshold choice is based on the noise value.

3. Applying a 2-pixel Gaussian sliding filter to make particle image shapes more regular.

The acquisition frequency needed to count all particles passing through the RoI is $\nu^* = 1/\Delta t_{RoI}$. Considering particles moving at approximately 2 km/s, the necessary acquisition frequency ν^* is in the order of 100 kHz. The result is therefore severely under-sampled, as the laser's repetition rate is 15 Hz. Moreover, the so-found particle count $n_p(t)$ represents the particles that pass through the laser sheet only, and no information is known about particles outside the laser sheet. Therefore, the obtained particle count should be considered only a qualitative indicator of the overall particle flux. The obtained n_p values can be used only in the hypothesis of homogeneous seeding.

4.5. Error sources

The systematic error sources of this experimental setup are here described and quantified:

- *Mechanical vibrations*: the wind tunnel might generate vibrations that cause optics misalignment and image shift. To assess this, the sample support structure was monitored in the raw data for any image displacement before, during, or after the tests. Owing to the massive structure of the L2K wind tunnel and its relatively low mass flow rate, no vibrations were detected. Therefore, no systematic error is introduced by mechanical vibrations.
- *Laser and optics misalignments*: the laser line-of-sight and the optics may randomly misalign due to mechanical vibrations and instabilities. However, precise monitoring of the laser status before and during each test, combined with the absence of mechanical vibrations, ensured that no systematic error was introduced.
- *Pixel quantization (finite sensor resolution)*: the sCMOS sensor resolution is 44.0 px/mm for this setup [13]. The location algorithm of LPT is based on the intensity-weighted method, thereby reducing the quantization error to 1/10 of pixel [40]. The quantization error is therefore 1/440 mm.
- *Intrinsic calibration uncertainty*: calibration is performed with the DaVis software [39] by third-order polynomial fit, whose error is less than 1.3 pixels for all experiments (i.e. 0.030 mm).

The overall systematic error on the LPT data is therefore 0.030 mm. Beyond systematic errors, the LPT algorithm can introduce a positional uncertainty due to its intensity-weighted profile detection. To control this, any measurement with a standard deviation exceeding 0.3 mm is discarded as an outlier, ensuring that the location error remains below this threshold. The 0.3 mm threshold should be considered a conservative limit, likely overestimating the detection error for most data points. By combining systematic error and positional uncertainty, the overall error on the LPT data is therefore less than 0.3 mm.

5. Results

The described mathematical model was fitted to bounded LPT data ($|y| \leq 5$ mm),[4] with the particle number n_p measured as mentioned in Section 4.4, for each run of the experimental campaign. Fitting was performed by numerical integration of Eq. (15), with the following strategy:

1. The model is fitted to LPT data of FCs^{nP} with $n_p(t) = 0$, to retrieve $k = k_0$, $a = a_0$ and $b = b_0$.

[4] LPT measurements were restricted to the central region of the sample surface, where physical quantities remain uniform, allowing the thickness evolution to be considered effectively one-dimensional.

Table 3
Fitted model parameters for FCs^{nP}.

	FCI^{nP}	FCII^{nP}
a_0 [mm/s]	0.024	0.038
b_0 [mm]	−2.08	−1.17
k_0 [s^{-1}]	0.015	0.030

2. The model is then fitted to LPT data of FCs^{P}, with the measured $n_p(t)$. During the fitting process, k, a, and b, are bounded such that: $(k, a, b) = (k, a, b)_0 \pm 5\%$. The proportionality factor A is thus retrieved for each run with particles.

All 6 runs with particles are reported in Figs. 14 to 16, and Figs. 17 to 19, along with one exemplary run without particles. The figures present the raw LPT data for both the FCs^{nP} and FCs^{P}, along with their respective fits describing the thickness evolution. Additionally, the particle count n_p is shown using green colour scales in three forms: the raw n_p, the Gaussian-smoothed n_p, and regions identified as particle bursts—i.,e., areas where the smoothed n_p exceeds a threshold defined as the mean value of the smoothed n_p plus 1.2 times its standard deviation.

The parameters obtained after fitting in FCs^{nP} are presented in Table 3. By comparing the two flow conditions, one can see that the higher heat load provided by FCII^{nP} affects the parameters' values: in the higher enthalpy flow condition, the long-term recession rate a_0 is higher, the swelling amount is lower in magnitude, and the system stiffness is higher—meaning that the response to the forcing term $Y_{eq}(t)$ is faster. The evaluated values of a_0, which are in agreement with the typical recession rate of cork-based ablators, should be appreciated. However, at this stage of the study there is a considerable uncertainty on the determination of a_0 in the lower-enthalpy flow condition, due to the short test times that did not allow the observation of the constant long-term recession rate, characteristic of cork-based ablators. Further campaigns are needed to study these parameters in a broad range of wind tunnel conditions and cork materials, to assess their variability. The outcome of a broad study aimed at the characterization of different materials in several flow conditions could be used by the scientific community to develop simple and fast mathematical models for the prediction of the ablation process.

By comparing Fig. 14 with Fig. 17, one can observe that the particle count is notably lower in the higher enthalpy flow condition. This is due to the agglo-melting phenomenon—particle agglomeration favoured by melting—theorized in [13]. Agglo-melting happens only in FCII^{P}, as the reservoir temperature of this flow condition is higher than the particle melting temperature. Moreover, all n_p profiles are not homogeneous and present significant variations: particle flow might be characterized by bursts and is significantly influenced by the particle seeding generator dynamics. Future studies should aim at improving this hardware component.

In Fig. 16, run 4 had less violent particle bursts, causing a less-pronounced thickness evolution, compared to runs 2 and 3. In runs 2 and 3, on the other hand, the first 20 s were highly loaded with particles that caused violent erosion. This phenomenon did not start at the beginning of the highly-loaded phase due to the fact that the material requires a start-up time to develop a brittle char layer. The model well fits run 4 and has a slight error at the beginning of runs 2 and 3; this might be due to the fact that the current mathematical model considers no start-up processes in terms material properties, which are hypothesized constant throughout the test. Nevertheless, it well represents the erosion events recorded with LPT, such as for example the one in run 3 at $t = 31$ s. The computed factors A are coherent between FCI^{P} runs, with an average value of $A = 5.211\text{e}{-5} \pm 3.5\%$.

In Figs. 17 to 19, the model well represents runs 8 and 9, while it has a slight deviation at the beginning of run 7, probably for the same reason mentioned for the previous figure (i. e. the material response

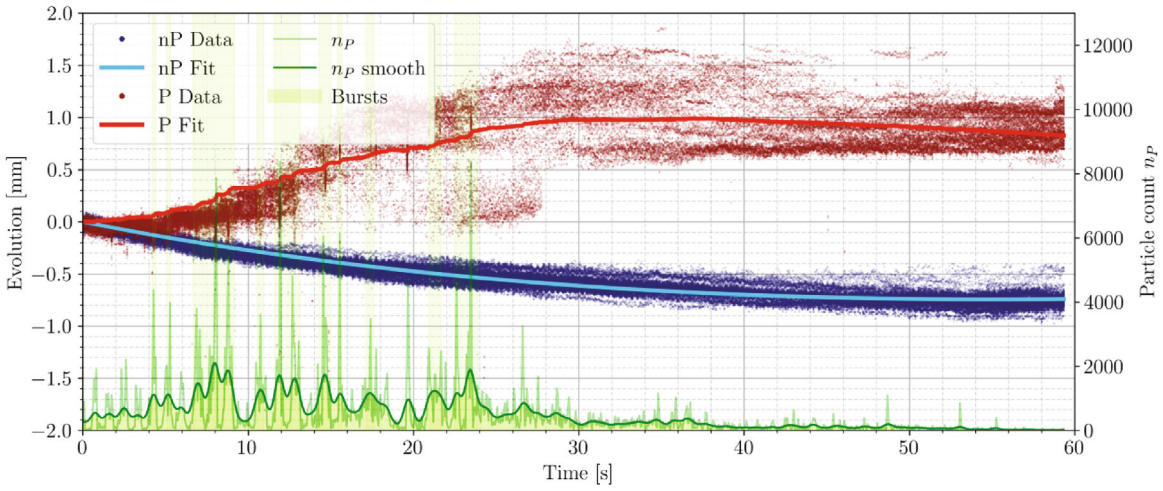

Fig. 14. Lower enthalpy FCI$^{P/nP}$: blue colours indicate conditions without particles (Run 1) and red colours indicate conditions with particles (Run 2, with computed A = 5.468e−5). The particles counted within the light sheet are presented in green, through raw data, Gaussian-smoothed results, and burst regions. (For interpretation of the references to colour in this figure legend, the reader is referred to the web version of this article.)

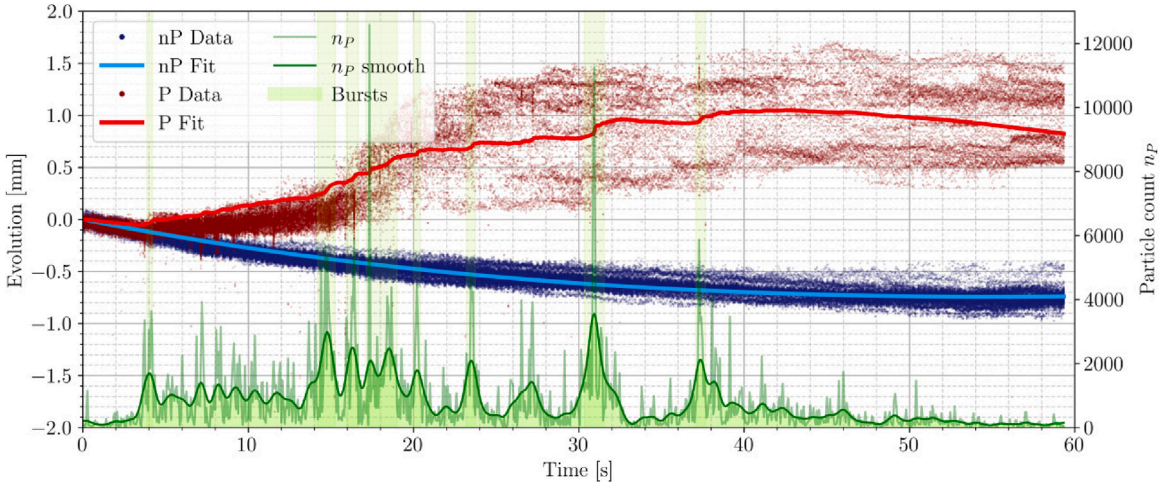

Fig. 15. Lower enthalpy FCI$^{P/nP}$: blue colours indicate conditions without particles (Run 1) and red colours indicate conditions with particles (Run 3, with computed A = 5.078e−5). The particles counted within the light sheet are presented in green, through raw data, Gaussian-smoothed results, and burst regions. (For interpretation of the references to colour in this figure legend, the reader is referred to the web version of this article.)

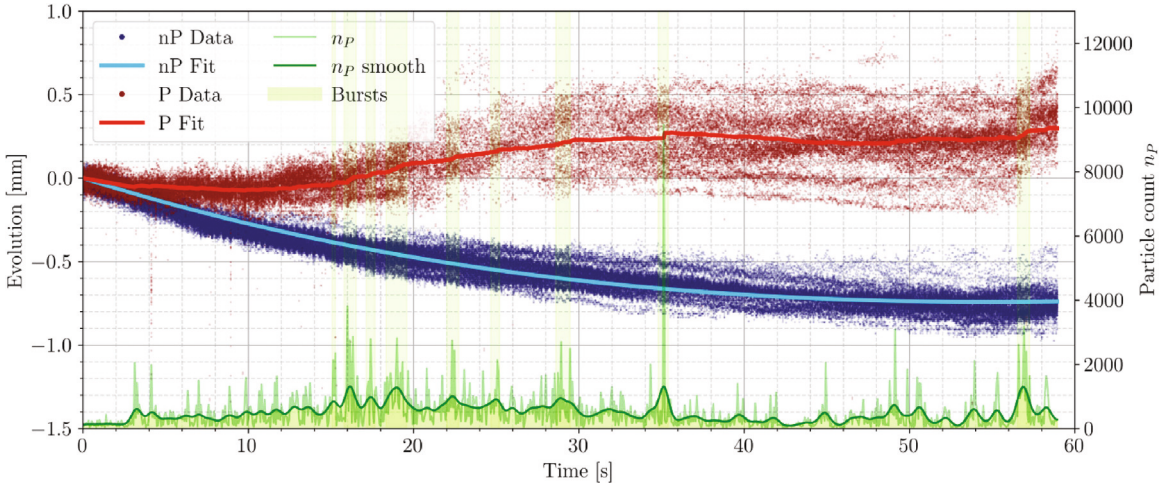

Fig. 16. Lower enthalpy FCI$^{P/nP}$: blue colours indicate conditions without particles (Run 1) and red colours indicate conditions with particles (Run 4, with computed A = 5.086e−5). The particles counted within the light sheet are presented in green, through raw data, Gaussian-smoothed results, and burst regions. (For interpretation of the references to colour in this figure legend, the reader is referred to the web version of this article.)

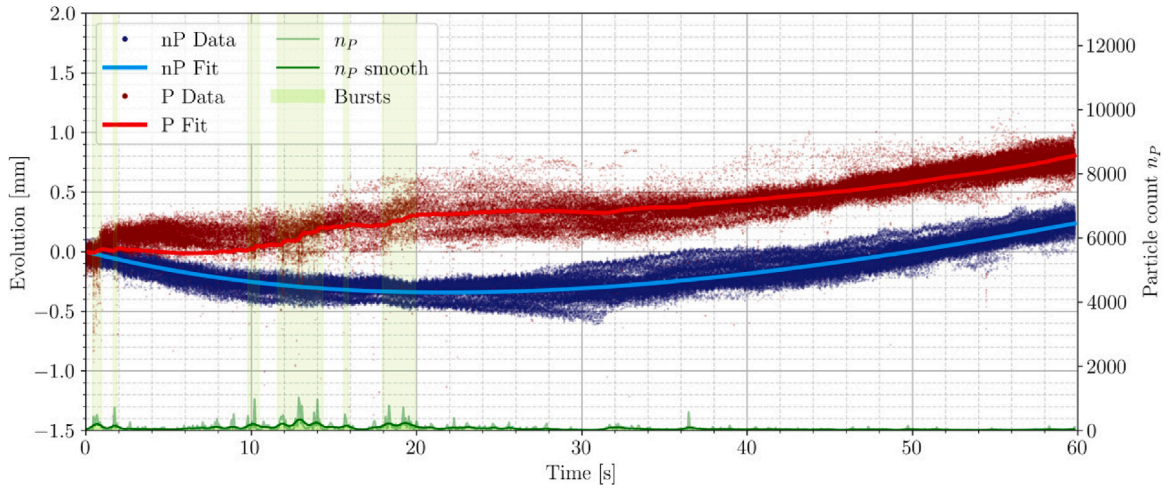

Fig. 17. Higher enthalpy FCII$^{P/nP}$: blue colours indicate conditions without particles (Run 5) and red colours indicate conditions with particles (Run 7, with computed A = 3.191e−4). The particles counted within the light sheet are presented in green, through raw data, Gaussian-smoothed results, and burst regions. (For interpretation of the references to colour in this figure legend, the reader is referred to the web version of this article.)

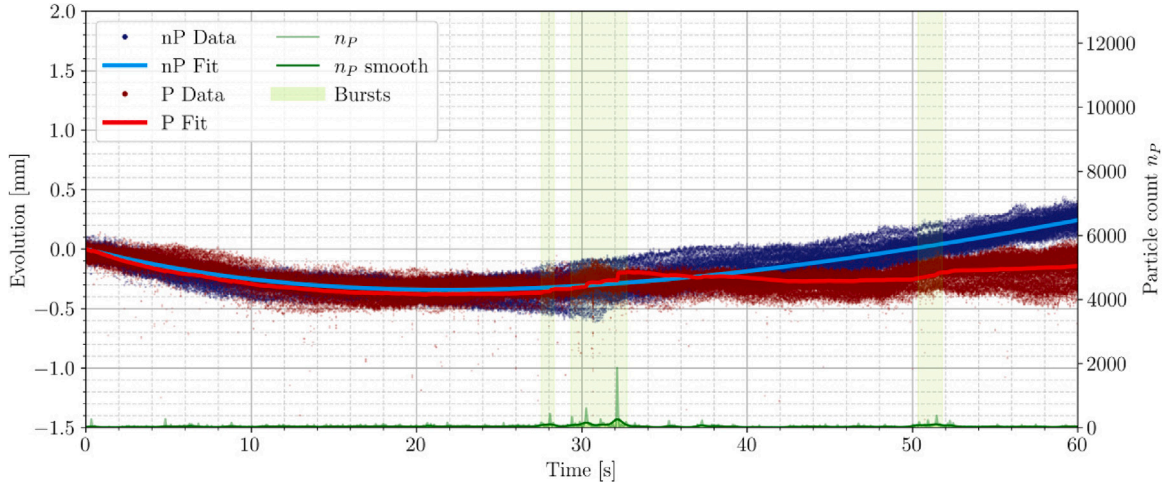

Fig. 18. Higher enthalpy FCII$^{P/nP}$: blue colours indicate conditions without particles (Run 5) and red colours indicate conditions with particles (Run 8, with computed A = 4.761e−4). The particles counted within the light sheet are presented in green, through raw data, Gaussian-smoothed results, and burst regions. (For interpretation of the references to colour in this figure legend, the reader is referred to the web version of this article.)

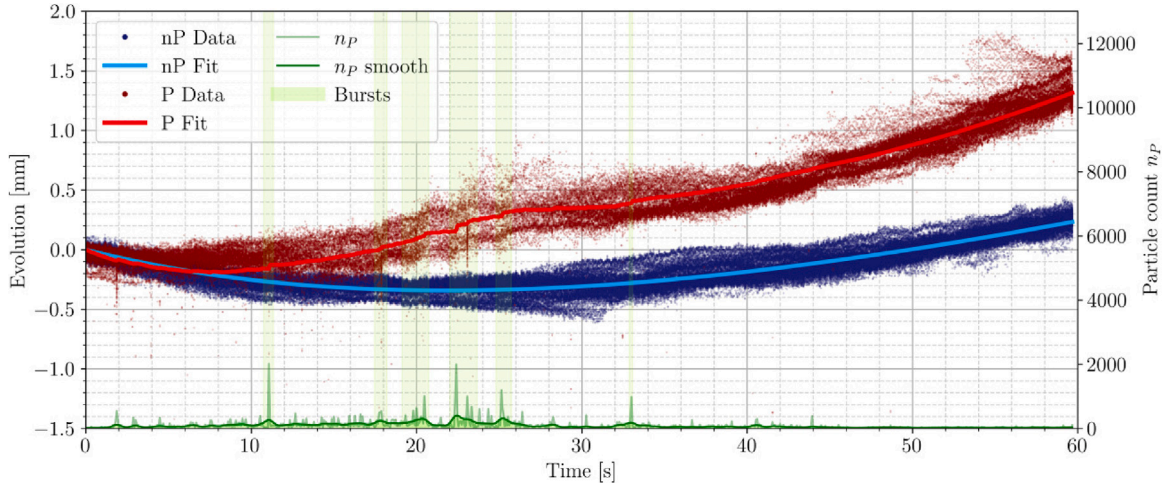

Fig. 19. Higher enthalpy FCII$^{P/nP}$: blue colours indicate conditions without particles (Run 5) and red colours indicate conditions with particles (Run 9, with computed A = 2.540e−4). The particles counted within the light sheet are presented in green, through raw data, Gaussian-smoothed results, and burst regions. (For interpretation of the references to colour in this figure legend, the reader is referred to the web version of this article.)

start-up processes). Most notably, run 8 had a very small particle flux, that did not cause any pronounced erosion effect, except at $t = 31$ s and $t = 51$ s. On the contrary, post-erosion swelling caused the probe to be more swollen than in the case without particles. The model well fits this behaviour and is thus a confirmation that post-erosion swelling may be a physical effect—which was never mentioned in the literature, regarding two-phase high-enthalpy flows effects on materials. A values are not coherent between FCII^P runs, as seen through the standard deviation: $A = 3.497\text{e}{-4} \pm 26.7\%$. The high deviation between the computed factors A can be another evidence of agglo-melting, that causes particle size distribution change. This requires dropping the hypotheses which the mathematical model is based on, and the analysis can be considered only qualitative for FCII^P.

FCI^P: $\boxed{A = 5.211 \times 10^{-5} \pm 3.5\%}$

FCII^P: $\boxed{A = 3.497 \times 10^{-4} \pm 26.7\%}$

Since these tests were too short to accurately characterize the long-term recession rate a and the swelling constant b, these results are not reported. In the future, longer tests shall be performed to evaluate these parameters with more accuracy. This analysis could have a broad application in future experimental campaigns, as it can be applied to tests with and without particles, for all possible atmospheres.

6. Conclusions

A one-dimensional mathematical model has been proposed to describe the thickness evolution of cork-based ablators in particle-laden two-phase high-enthalpy flows, explicitly accounting for swelling, recession, particle-induced erosion, and the newly identified post-erosion swelling phenomenon. The thickness evolution is described by a constrained initial value problem defined and discussed in Section 3, whose solution explicitly depends on the four terms related to recession, swelling, post-erosion swelling and particle-induced erosion, as reported in Eq. (17).

Fitting against time-resolved thickness evolution data demonstrated that the model reliably reproduces experimental results within acceptable accuracy, thereby confirming the existence of post-erosion swelling. The experimental setup, which accounts for time-resolved thickness evolution measurements via laser-sheet profile tracking (LPT) and particle counting, is described in Section 4, while the corresponding fitting results are presented in Section 5.

Depending on the heat flux condition, the long-term recession rate a ranges from 0.024 mm/s to 0.038 mm/s, the swelling parameter b from -2.08 mm to -1.17 mm, and the system's stiffness k from 0.015 s^{-1} to 0.030 s^{-1}, as reported in Table 3. The particle-induced erosion parameter A has physical significance under the assumptions of constant and homogeneous particle velocity, constant particle and material properties, homogeneous seeding, and quasi-perpendicular impact. These conditions are satisfied only in FCI^P, where $A = 5.211 \times 10^{-5} \pm 3.5\%$. In FCII^P, however, particles undergo agglomeration and melting, which violates the assumption of constant particle properties; consequently, the analysis in this case can only be considered qualitative.

Experiments were conducted in the arc-heated wind tunnel L2K under four flow conditions (Table 1), which correspond to two heat flux levels (Table 2) representative of Martian entry, including dust storms. Given the limited number of investigated flow conditions and heat flux points, caution must be exercised when extrapolating the model parameters.

6.1. Outlook

This paper offers a computationally efficient basis for the determination of material-specific parameters and provides a foundation for future parametric extensions aimed at predictive modelling of material response in high-enthalpy flow environments, including scenarios relevant to Martian atmospheric entry during dust storms.

Further experimental campaigns should be conducted to explore a wider range of conditions and materials, with the ultimate aim of deriving parameter sets that allow computationally efficient predictions of cork behaviour—applicable, for example, to both Earth and Martian atmospheric entry—using the model developed in this work. This will also enable a systematic sensitivity analysis of the model parameters with respect to flow conditions and heat flux.

In the future, microscopic structural analysis (e.g., Scanning Electron Microscope SEM combined with Energy-Dispersive X-ray spectroscopy EDX) could be performed to further elucidate the physical mechanisms of post-erosion swelling. The feasibility of this analysis with respect to test operation and physical limits imposed by arc-heated flow operation should be assessed.

CRediT authorship contribution statement

Ciro Salvi: Writing – review & editing, Writing – original draft, Visualization, Software, Methodology, Investigation, Formal analysis, Data curation, Conceptualization. **Oliver Hohn:** Writing – review & editing, Supervision, Project administration. **Ali Gülhan:** Writing – review & editing, Supervision, Resources, Project administration, Funding acquisition.

Declaration of competing interest

The authors declare that they have no known competing financial interests or personal relationships that could have appeared to influence the work reported in this paper.

Acknowledgements

This project is funded by the DLR's Program Directorate for Space Research and Development. The authors would like to thank Prof. Isaac Boxx from RWTH Aachen for his valuable scientific inputs, Amorim Cork Solutions for providing the samples for free, and the staff from the Supersonic and Hypersonic Technologies Department in DLR Köln.

Data availability

Data will be made available on request.

References

[1] T. Reimer, C. Zuber, J. Rieser, T. Rothermel, Determination of the mechanical properties of the lightweight ablative material Zuram, in: N.P. Bansal, R.H. Castro, M. Jenkins, A. Bandyopadhyay, S. Bose, A. Bhalla, J.P. Singh, M.M. Mahmoud, G. Pickrell, S. Johnson (Eds.), Processing, Properties, and Design of Advanced Ceramics and Composites II: Ceramic Transactions, Cambridge Scholars Publishing, The American Ceramic Society, 2017, p. ch. 28.

[2] R.A.S. Beck, D.M. Driver, M.J. Wright, H.H. Hwang, K.T. Edquist, S.A. Sepka, Development of the Mars Science Laboratory heatshield thermal protection system, J. Spacecr. Rockets 51 (2014) 4.

[3] M. Stackpole, D. Kao, V. Qu, G. Gonzales, Post-flight evaluation of PICA and PICA-X - Comparisons of the stardust SRC and Space-X dragon 1 forebody heatshield materials, in: International Planetary Probe Workshop, San Jose, California, 18-21 Jun, 2013.

[4] E. Stern, M. Mahzari, Dragonfly TPS sizing and analysis, in: AIAA SciTech, National Harbor, Maryland, 23-27 Jan, 2023.

[5] J.E. Pavlosky, L.G.S. Leger, Apollo Experience Report - Thermal Protection Subsystem, Technical Note NASA TN D-7564, NASA Lyndon B. Johnson Space Center, Houston, Texas, 1974.

[6] A.P. Santos, L.J. Abbott, J.B. Haskins, Fracture of charring Avcoat with mesh-free material response-coupled fracture approach, in: 13th Ablation Workshop, Mountain View, California, 7-9 Nov., 2023.

[7] F.S. Milos, Y.K. Chen, W.M. Congdon, J.M. Thornton, Mars pathfinder entry temperature data, aerothermal heating, and heatshield material response, J. Spacecr. Rockets 36 (1999) 3.

[8] A.J. Ball, T. Blancquaert, O. Bayle, L.V. Lorenzoni, A.F. Haldemann, S.E. Team, The ExoMars schiaparelli entry, descent and landing demonstrator module (EDM) system design, Space Sci. Rev. 218 (2022) 44.

[9] I. Sakraker, O. Chazot, J.P. Carvalho, Performance of cork-based thermal protection material P50 exposed to air plasma, CEAS Space J. 15 (2022) 377–393.
[10] M. Cioeta, G. Di Vita, T. Signorelli Maria, G. Bianco, M. Cutroni, F. Damiani, V. Ferretti, A. Rotondo, Design, qualification, manufacturing and integration of IXV ablative thermal protection system, Acta Astronaut. 124 (2016) 90–101.
[11] C. Salvi, O. Hohn, A. Gülhan, Laser-based recession measurement and thermal characterization of ablator in particle-laden martian flow, AIAA J. (minor Review requested) xx, xx.
[12] C. Salvi, A. Gülhan, Velocity measurements in particle-laden high-enthalpy flow using non-intrusive techniques, Exp. Fluids 65 (2024) 39.
[13] C. Salvi, A. Gülhan, PIV in the vicinity of cork samples in particle-laden high-enthalpy flow, Exp. Fluids 66 (2025) 160.
[14] C. Salvi, L. Steffens, O. Hohn, A. Gülhan, F. Maggi, Martian flow characterization using tunable diode laser absorption spectroscopy, in high enthalpy facilities, Acta Astronaut. 213 (2023) 204–214.
[15] K. Keller, P. Lindenmaier, E.K. Pfeiffer, B. Esser, A. Gülhan, P. Omaly, M. Desjean, Dust particle erosion during Mars entry, in: 40th International Conference on Environmental Systems, Barcelona, Spain, 11-15 Jul., 2010.
[16] G. Palmer, A. Sahai, D. Allofs, A. Gülhan, Comparing particle flow regimes in the L2K arcjet with Martian entry conditions, in: 2nd International Conference on Flight Vehicles, Aerothermodynamics and Re-Entry Missions and Engineering, Heilbronn, Germany, 19-23 Jun., 2022.
[17] A. Mazzarecchio, One-dimensional thermal analysis model for charring ablative materials, J. Aerosp. Technol. Manag. 10 (2018) 965.
[18] M. Rivier, J. Lachaud, P. Congedo, Ablative thermal protection system under uncertainties including pyrolysis gas composition, Aerosp. Sci. Technol. 84 (2019) 1059–1069.
[19] K. Price, S. Bailey, A. Martin, Characterization and modeling of spallation in thermal protection systems, in: 11th International Conference on Computational Fluid Dynamics, Maui, Hawaii, 11-15 Jul, 2022.
[20] D.M. Driver, M.W. Olson, M.D. Bernhardt, M. MacLean, Understanding high recession rates of carbon ablators seen in shear tests in an arc jet, in: 48th AIAA Aerospace Sciences Meeting, Orlando, Florida, 4-7 Jan, 2010.
[21] R.A.S. Beck, Ablative thermal protection system fundamentals, in: IPPW, San Jose, California, 15-21 Jun, 2013.
[22] G. Bailet, A. Denis, A. Bourgoing, C.O. Laux, T.E. Magin, Nonintrusive instrument for thermal protection system to measure recession and swelling, J. Spacecr. Rockets 59 (2022) 1.
[23] Y.V. Polezhaev, Stabilization of the erosion process affecting the material of a barrier under repetitive impact by particles, Transl. from Inzhenerno-Fizicheskii Zhurnal 37 (1979) 3.
[24] Y.V. Polezhaev, V.I. Panchenko, Fundamental relations of erosion kinetics, J. Eng. Phys. 52 (1987) 507–512.
[25] M. Hufnagel, S. Staudacher, C. Koch, Experimental and numerical investigation of the mechanical and aerodynamic particle size effect in high-speed erosive flows, J. Eng. Gas Turbines Power 140 (2018) 102604.
[26] G.C. Lorenz, Simulation of the erosive effects of multiple particle impacts in hypersonic flow, J. Spacecr. 7 (1970) 2.
[27] M. Hufnagel, C. Werner-Spatz, C. Koch, S. Staudacher, High-speed shadowgraphy measurements of an erosive particle-laden jet under high-pressure compressor conditions, J. Eng. Gas Turbines Power 140 (2018) 012604.
[28] Y.I. Oka, K. Okamura, T. Yoshida, Practical estimation of erosion damage caused by solid particle impact. Part 1: Effects of impact parameters on a predictive equation, Wear 259 (2005) 95–101.
[29] Y.I. Oka, T. Yoshida, Practical estimation of erosion damage caused by solid particle impact. Part 2: Mechanical properties of materials directly associated with erosion damage, Wear 259 (2005) 102–109.
[30] G. Palmer, E. Ching, M. Ihme, D. Allofs, A. Gülhan, Modeling heat-shield erosion due to dust particle impacts for Martian entries, J. Spacecr. Rockets 57 (2020) 857–875.
[31] P- Papadopoulos, M.E. Tauber, I. Chang, Heatshield erosion in a dusty Martian atmosphere, J. Spacecr. Rockets 30 (1993) 2.
[32] S.R. Dominik, Development of a Thermal Ablation Model with Experimental Validation in an Arc-Heated Wind Tunnel, RWTH Aachen, DLR, 2023.
[33] K.B. Thompson, C.O. Johnston, B. Kleb, A. Mazaheri, T.K. West, W.A. Wood, LAURA Users Manual: 5.7, Technical Report TM-2020-220566, NASA Langley, Hampton, 2024.
[34] C.O. Johnston, P.A. Gnoffo, A. Mazaheri, Study of ablation-flowfield coupling relevant to the orion heatshield, AIAA J. Thermophys. Heat Transf. 26 (2013) 2.
[35] E. Farbar, H. Alkandry, J. Wiebenga, I.D. Boyd, Simulation of ablating hypersonic vehicles with finite-rate surface chemistry, in: 11th AIAA/ASME Joint Thermophysics and Heat Transfer Conference, Atlanta, Georgia, 16 - 20 Jun., 2014.
[36] ESA, ExoMars 2016 Schiaparelli descent sequence, 2022, https://exploration.esa.int/web/mars/-/57465-exomars-2016-schiaparelli-descent-sequence. (Accessed: 22 July 2022).
[37] W.L. Bade, J.M. Yos, The NATA Code - Theory and Analysis, Technical Report CR-2547, NASA, 1975.
[38] M. Mahzari, R.D. Braun, T.R. White, D. Bose, Inverse estimation of the Mars Science Laboratory entry aeroheating and heatshield response, J. Spacecr. Rockets 52 (2015) 4.
[39] LaVision DaVis, https://www.lavision.de/en/products/davis-software/. (Accessed: 01 January 2025).
[40] J.A. Cox, Evaluation of peak location algorithms with subpixel accuracy for mosaic focal planes, in: Processing of Images and Data from Optical Sensors, vol. 292, 1981.